12-21-2021

CCR2 signaling restricts SARS-CoV-2 infection

Abigail Vanderheiden

Jeronay Thomas

Allison L Soung

Meredith E Davis-Gardner

Katharine Floyd

See next page for additional authors

Authors

Abigail Vanderheiden, Jeronay Thomas, Allison L Soung, Meredith E Davis-Gardner, Katharine Floyd, Fengzhi Jin, David A Cowan, Kathryn Pellegrini, Pei-Yong Shi, Arash Grakoui, Robyn S Klein, Steven E Bosinger, Jacob E Kohlmeier, Vineet D Menachery, and Mehul S Suthar

CCR2 Signaling Restricts SARS-CoV-2 Infection

Abigail Vanderheiden,[a,b,c] Jeronay Thomas,[d,e] Allison L. Soung,[f] Meredith E. Davis-Gardner,[a,b,c] Katharine Floyd,[a,b,c] Fengzhi Jin,[b,c,d] David A. Cowan,[b,c,h] Kathryn Pellegrini,[b,c,h] Adrian Creanga,[l] Amarendra Pegu,[l] Alexandrine Derrien-Colemyn,[l] Pei-Yong Shi,[g] Arash Grakoui,[b,c,d] Robyn S. Klein,[f,i,j] Steven E. Bosinger,[b,c,h] Jacob E. Kohlmeier,[d,e] (iD) Vineet D. Menachery,[k] (iD) Mehul S. Suthar[a,b,c,e]

aCenter for Childhood Infections and Vaccines of Children's Healthcare of Atlanta, Department of Pediatrics, Emory University School of Medicine, Atlanta, Georgia, USA

bEmory Vaccine Center, Emory University, Atlanta, Georgia, USA

cYerkes National Primate Research Center, Atlanta, Georgia, USA

dDepartment of Microbiology and Immunology, Emory University, Atlanta, Georgia, USA

eEmory-UGA Center of Excellence of Influenza Research and Surveillance (CEIRS), Atlanta, Georgia, USA

fCenter for Neuroimmunology and Neuroinfectious Diseases, Department of Medicine, Washington University School of Medicine, St. Louis, Missouri, USA

gDepartment of Biochemistry and Molecular Biology, The University of Texas Medical Branch, Galveston, Texas, USA

hDepartment of Pathology and Laboratory Medicine, Emory University School of Medicine, Atlanta, Georgia, USA

iDepartment of Pathology and Immunology, Washington University School of Medicine, St. Louis, Missouri, USA

jDepartment of Neurosciences, Washington University School of Medicine, St. Louis, Missouri, USA

kDepartment of Microbiology and Immunology, Institute for Human Infection and Immunity, World Reference Center for Emerging Viruses and Arboviruses, University of Texas Medical Branch, Galveston, Texas, USA

lVaccine Research Center, National Institute of Allergy and Infectious Diseases, National Institutes of Health, Bethesda, Maryland, USA

ABSTRACT Severe acute respiratory syndrome coronavirus 2 (SARS-CoV-2) has caused a historic pandemic of respiratory disease (coronavirus disease 2019 [COVID-19]), and current evidence suggests that severe disease is associated with dysregulated immunity within the respiratory tract. However, the innate immune mechanisms that mediate protection during COVID-19 are not well defined. Here, we characterize a mouse model of SARS-CoV-2 infection and find that early CCR2 signaling restricts the viral burden in the lung. We find that a recently developed mouse-adapted SARS-CoV-2 (MA-SARS-CoV-2) strain as well as the emerging B.1.351 variant trigger an inflammatory response in the lung characterized by the expression of proinflammatory cytokines and interferon-stimulated genes. Using intravital antibody labeling, we demonstrate that MA-SARS-CoV-2 infection leads to increases in circulating monocytes and an influx of CD45+ cells into the lung parenchyma that is dominated by monocyte-derived cells. Single-cell RNA sequencing (scRNA-Seq) analysis of lung homogenates identified a hyperinflammatory monocyte profile. We utilize this model to demonstrate that mechanistically, CCR2 signaling promotes the infiltration of classical monocytes into the lung and the expansion of monocyte-derived cells. Parenchymal monocyte-derived cells appear to play a protective role against MA-SARS-CoV-2, as mice lacking CCR2 showed higher viral loads in the lungs, increased lung viral dissemination, and elevated inflammatory cytokine responses. These studies have identified a potential CCR2-monocyte axis that is critical for promoting viral control and restricting inflammation within the respiratory tract during SARS-CoV-2 infection.

IMPORTANCE SARS-CoV-2 has caused a historic pandemic of respiratory disease (COVID-19), and current evidence suggests that severe disease is associated with dysregulated immunity within the respiratory tract. However, the innate immune mechanisms that mediate protection during COVID-19 are not well defined. Here, we characterize a mouse model of SARS-CoV-2 infection and find that early CCR2-dependent infiltration of monocytes restricts the viral burden in the lung. We find that SARS-CoV-2 triggers an inflammatory response in the lung characterized by the expression of proinflammatory cytokines and interferon-stimulated genes. Using RNA sequencing and flow cytometry approaches, we demonstrate that SARS-CoV-2 infection leads to increases in circulating monocytes and an influx of CD45+

cells into the lung parenchyma that is dominated by monocyte-derived cells. Mechanistically, CCR2 signaling promoted the infiltration of classical monocytes into the lung and the expansion of monocyte-derived cells. Parenchymal monocyte-derived cells appear to play a protective role against MA-SARS-CoV-2, as mice lacking CCR2 showed higher viral loads in the lungs, increased lung viral dissemination, and elevated inflammatory cytokine responses. These studies have identified that the CCR2 pathway is critical for promoting viral control and restricting inflammation within the respiratory tract during SARS-CoV-2 infection.

KEYWORDS lung inflammation, monocytes, SARS-CoV-2, innate immunity, mouse model

Severe acute respiratory syndrome coronavirus 2 (SARS-CoV-2) is a novel betacoronavirus that emerged in Wuhan, China, in December 2019 and is the causative agent of coronavirus disease 2019 (COVID-19) (1, 2). Innate immunity to SARS-CoV-2 begins with a limited interferon (IFN) response and the production of inflammatory cytokines (interleukin-6 [IL-6], IL-1β, tumor necrosis factor alpha [TNF-α], and IL-8) by respiratory epithelial cells or alveolar macrophages (3–7). As shown in bronchoalveolar lavage (BAL) fluids of COVID-19 patients, this innate immune response coincides with robust infiltration of neutrophils, monocytes, and dendritic cells (DCs) into the lung airways (6, 8). Monocytes in the lung parenchyma can be divided into subpopulations characterized by their expression of Ly6C: Ly6C-high classical monocytes are proinflammatory, whereas Ly6C-low nonclassical monocytes promote wound healing (9, 10). Ly6C-low monocytes are prevalent under homeostatic conditions; however, after viral infection, Ly6C-high monocytes will infiltrate the lung in a CCR2-dependent manner (10–12). Classical Ly6C-high monocytes can differentiate into monocyte-derived dendritic cells (moDCs), which increase in number in response to viral respiratory infection, produce type I IFN, and excel at antigen presentation (13). The contribution of monocytes to the promotion of protective immunity to SARS-CoV-2 infection is not known. In this study, we utilize a mouse-adapted SARS-CoV-2 (MA-SARS-CoV-2) strain and the human variant B.1.351 to evaluate the contribution of monocytes to protective immunity against SARS-CoV-2 and identify a CCR2-monocyte axis that is critical for promoting viral control and restricting inflammation within the respiratory tract during SARS-CoV-2 infection.

RESULTS

Variant B.1.351 and MA-SARS-CoV-2 replicate in the lungs of C57BL/6 mice. To investigate the immunological response to SARS-CoV-2 in the lung, we generated an MA-SARS-CoV-2 strain (see Fig. S1A in the supplemental material). We engineered mutations into the infectious clone (ic) SARS-CoV-2 backbone (14) that have been shown to increase SARS-CoV-2 virulence in mice (15). Next, this virus was serially passaged 20 times in the lungs of BALB/c mice. Deep sequencing of plaque-isolated virus revealed three additional acquired mutations, which include two within the spike (K417N and H655Y) and one within the envelope (E8V) gene. Next, we confirmed the utility of MA-SARS-CoV-2 as a model to study SARS-CoV-2 pathogenesis in C57BL/6 mice. Intranasally infected mice survived infection with MA-SARS-CoV-2 but had 10% body weight loss at days 2 to 3 postinfection (p.i.) (Fig. 1A). Lung tissue was harvested at 0, 2, and 4 days p.i., and infectious MA-SARS-CoV-2 was measured via a plaque assay. MA-SARS-CoV-2 titers peaked at day 2 p.i., with 10^9 PFU per g of lung tissue. Viral RNA peaked in the lung at day 2 p.i., dropping 100-fold by day 4 p.i. (Fig. 1B). To determine the localization of MA-SARS-CoV-2 in the lung, we performed *in situ* hybridization (ISH) using probes that target the spike gene of SARS-CoV-2. Viral RNA was restricted to cells lining the airways of the lung, in accordance with observations in humans (Fig. 1C) (16). Examination of the antiviral response to MA-SARS-CoV-2 in the lung found that the expression of *Ifnl2* and interferon-stimulated genes (ISGs) peaked at day 2 p.i. Chemokines (*Cxcl10*, *Ccl2*, and *Ccl5*) and endogenous pyrogens (*Il6*, *Tnf*, and *Il1b*) were upregulated in response to MA-SARS-CoV-2 infection in the lung (Fig. S1B). We next plotted the gene expression of representative transcripts against viral RNA and found
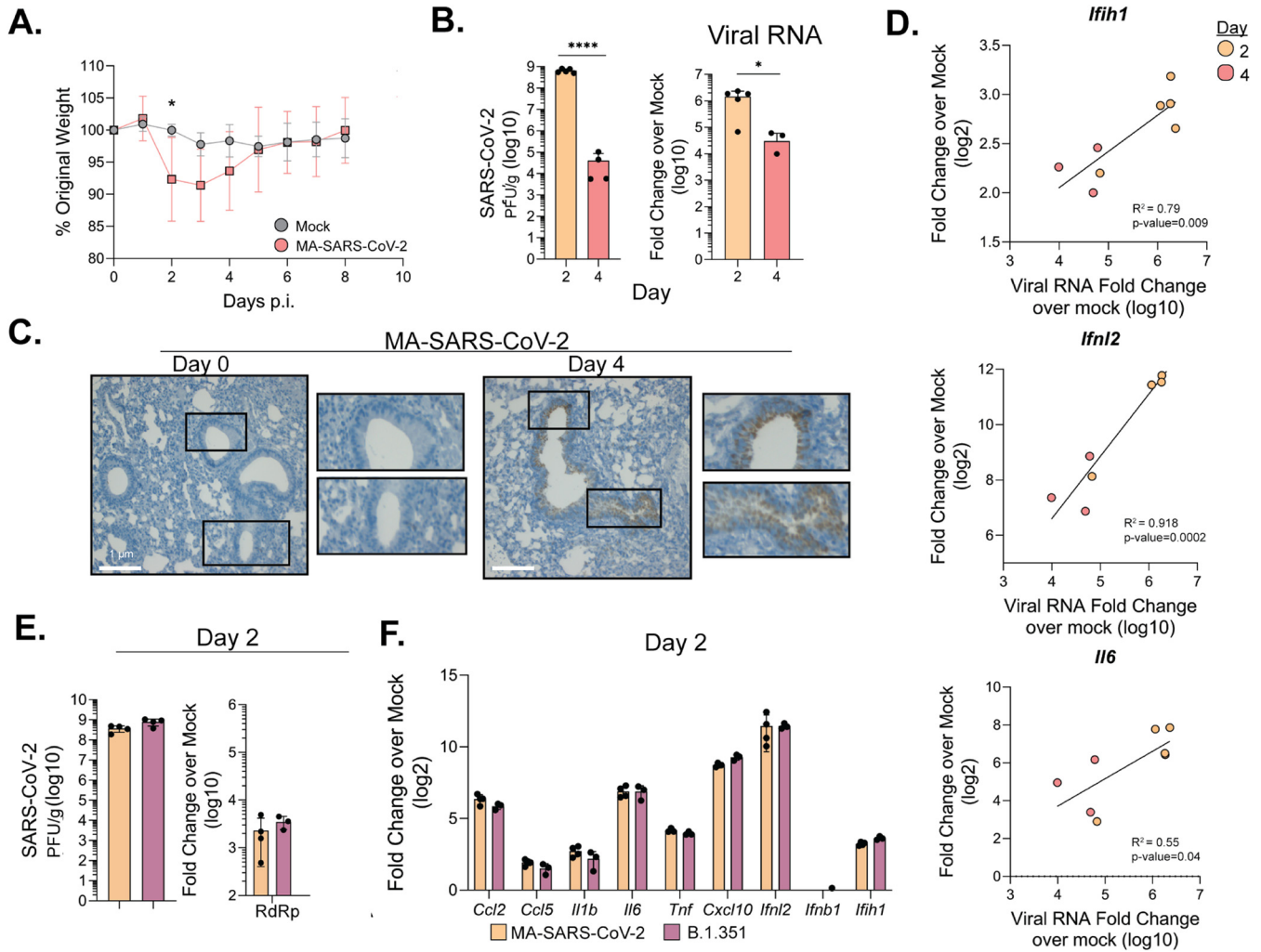
FIG 1 MA-SARS-CoV-2 and B.1.351 replicate in the respiratory tract. C57BL/6J mice were infected intranasally with 5×10^5 PFU of MA-SARS-CoV-2 or an equal volume of PBS for mock mice. (A) Percentage of initial weight for mock- and MA-SARS-CoV-2-infected mice over 8 days. (B) Quantification of MA-SARS-CoV-2 titers from lung tissue at the indicated day postinfection as measured by a plaque assay (left) or qRT-PCR (right). Threshold cycle (C_T) values are represented as relative fold changes over mock ($\log_{10}$). (C) *In situ* hybridization was performed using a probe for MA-SARS-CoV-2 spike protein RNA. Representative images of lung slices from mock or day 4 p.i. are shown. (D) The fold change over mock for the indicated gene was plotted against the corresponding MA-SARS-CoV-2 RNA for each sample, and linear regression was used to determine correlation. (E) Quantification of viral titers from lung tissue by a plaque assay at day 2 p.i. from mice infected with MA-SARS-CoV-2 or human variant B.1.351 (5×10^5 PFU/mouse). On the right is the quantification of the RNA-dependent RNA polymerase (RdRp) fold change over mock. (F) Gene expression measured via qRT-PCR for the indicated genes from lungs infected with MA-SARS-CoV-2 or B.1.351 at 2 days p.i. Results are representative of data from 2 independent experiments with 5 mice per group. Statistical significance was determined using unpaired Student's *t* tests or linear regression. *, $P < 0.05$; ****, $P < 0.0001$.

that *Ifih1*, *Ifnl2*, and *Il6* levels positively correlated with the MA-SARS-CoV-2 viral burden (Fig. 1D). Thus, MA-SARS-CoV-2 infects the respiratory tract and induces a viral load-dependent inflammatory response in C57BL/6 mice.

MA-SARS-CoV-2 contains several mutations, including three within the spike protein, at residues K417N and N501Y, which also appear in the SARS-CoV-2 B.1.351 variant (17). Next, we evaluated if a natural clinical isolate of B.1.351 could establish infection in mice. We intranasally inoculated C57BL/6 mice with 5×10^5 PFU of B.1.351 or MA-SARS-CoV-2 and found that B.1.351 replicated to high viral titers within lungs, as measured by plaque assays and quantitative reverse transcription-PCR (qRT-PCR) for RNA-dependent RNA polymerase (RdRp) RNA (Fig. 1E). The B.1.351 variant induced levels of cytokine and ISG expression similar to those induced by MA-SARS-CoV-2 in the lung at day 2 p.i. (Fig. 1F). Combined, these data demonstrate that the variant B.1.351 can infect C57BL/6 mice and replicates similarly to MA-SARS-CoV-2.

MA-SARS-CoV-2 infection induces hyperinflammatory monocytes and dysregulated alveolar macrophages. To investigate cellular innate immunity to SARS-CoV-2, we performed single-cell RNA sequencing (scRNA-Seq) on lung homogenates from day 0 or 4 after infection with MA-SARS-CoV-2 (4 mice per group). We obtained 9,399 cells at day 0 and 10,982 cells at day 4 p.i., and unbiased clustering identified 23 distinct groups comprised of T cells, B cells, DCs, epithelial (Epi) cells, neutrophils (Neut), natural killer (NK) cells, alveolar macrophages (AMs), and monocytes (mono). We further distinguished between inflammatory (Infl), nonclassical (NC), and intermediate (Tr) monocytes (Fig. 2A). MA-SARS-CoV-2 induced a decrease in the frequency of epithelial cells and increases in the frequencies of inflammatory monocytes and DCs in the lung (Fig. 2B).

We next mapped the expression of genes previously associated with COVID-19 progression to cell subsets in our MA-SARS-CoV-2 model (Fig. 2C). We noted low and sporadic expression levels of *Ifnb1* or *Ifnl2* but pronounced ISG expression, *Isg15* and *Irf7*, in alveolar macrophage, monocyte, and DC populations. Inflammatory cytokines were expressed primarily in neutrophils (*Il1b*) or monocytes (*Cxcl16*). Other markers associated with COVID-19 were also localized to neutrophil (*S100a8*) or monocyte (*Mmp14*) populations (Fig. 2C) (18). While the chemokine *Ccl2* was expressed primarily by inflammatory monocytes, the cognate receptor, *Ccr2*, was more widespread, with expression on monocytes, DCs, and NK cells (Fig. 2C). Gene set enrichment analysis (GSEA) of inflammatory monocyte populations identified an enrichment of inflammatory, interferon alpha, and interferon gamma response genes after MA-SARS-CoV-2 infection (Fig. 2D). Thus, MA-SARS-CoV-2 results in a proinflammatory response driven by neutrophils and inflammatory monocytes.

Alveolar macrophages showed changes in frequency after MA-SARS-CoV-2 infection (Fig. 2B). To further examine this population, we performed a heat map analysis of the top differentially expressed genes (DEGs) between mock- and MA-SARS-CoV-2-infected samples. MA-SARS-CoV-2 infection upregulated genes involved in antigen presentation (*B2m* and *H2-q7*), ISGs (*Ifi2712a* and *Oas1a*), and inflammatory cytokines (*Ccl9* and *Ccl6*) (Fig. 2E). We performed GSEA using a gene list enriched in alveolar macrophages from COVID-19 patients and found that alveolar macrophages from MA-SARS-CoV-2-infected mice had both a hyperinflammatory and suppressive signature (Fig. 2F) (6). Together, these data demonstrate that alveolar macrophages adopt a dysregulated profile in MA-SARS-CoV-2-infected mice.

Monocytes and monocyte-derived cells rapidly infiltrate the lung in response to MA-SARS-CoV-2 infection. Next, we investigated the cellular innate immune response to MA-SARS-CoV-2 at days 0, 2, and 4 p.i. Mice were intravitally labeled with CD45 conjugated to phycoerythrin (PE) to allow the identification of circulating (CD45$^+$ *in vivo*) and parenchymal (CD45$^-$ *in vivo*) cells in the lung. MA-SARS-CoV-2 infection initiated a stepwise increase in the total circulating and parenchymal CD45$^+$ cell infiltrate in the lung at days 2 and 4 p.i. (Fig. 3A; see Fig. S2 for the gating strategy). Granulocyte numbers were elevated in circulation at 2 and 4 days p.i. and infiltrated into the lung by day 2 p.i., with a 100-fold increase in parenchymal neutrophils (Fig. 3B; Fig. S3A). Circulating macrophage numbers were unchanged by infection; however, beginning at day 2 p.i., parenchymal macrophage numbers decreased compared to those in mock-infected mice (Fig. 3C). This downward trend appeared to be due to a sequential loss of alveolar macrophages at days 2 and 4 p.i. (Siglec-F$^+$ CD11c$^+$), while interstitial macrophages (CD11c$^-$ Siglec-F$^-$ Ly6C$^-$) were unaffected (Fig. 3D). At day 4 p.i., we observed a 100-fold increase in cells that expressed both macrophage markers, CD64 and F4/80, and monocyte markers, Ly6C and CD11b, which we designated "transitional macrophages" (Fig. 3D). All macrophages upregulated major histocompatibility complex class I (MHC-I) in response to MA-SARS-CoV-2, although the effect was more pronounced in transitional macrophages, which also upregulated CD86 (Fig. S3B and C). Together, these data identify a shift in the lung macrophage composition, with decreased numbers of alveolar macrophages and increased numbers of activated transitional macrophages during MA-SARS-CoV-2 infection.
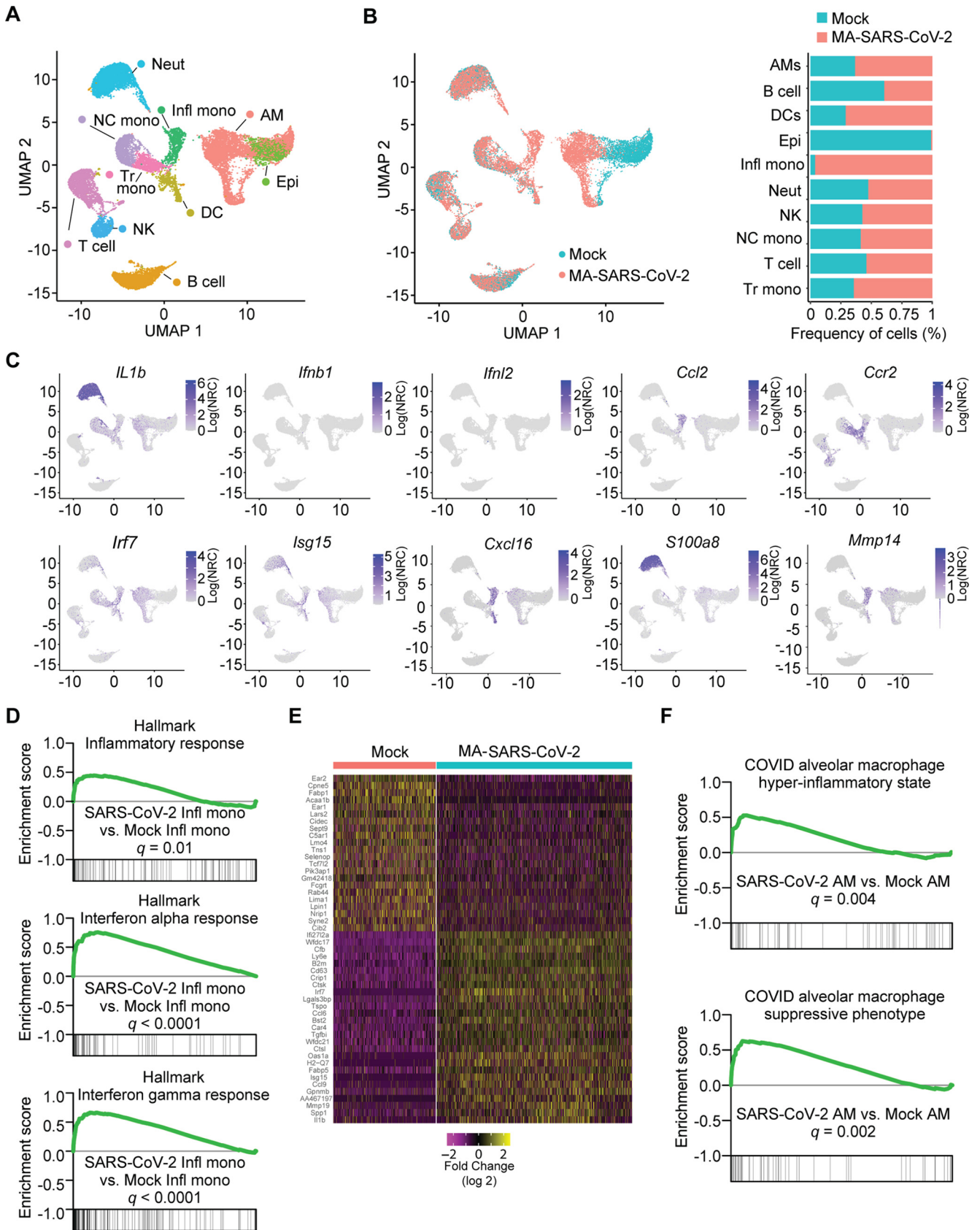
FIG 2 MA-SARS-CoV-2 induces hyperinflammatory monocytes and macrophages in the lung. C57BL/6 mice were infected with MA-SARS-CoV-2, and lungs were harvested at days 0 and 4 p.i., processed to a single-cell suspension, captured in droplets on a 10× chromium controller, and analyzed via
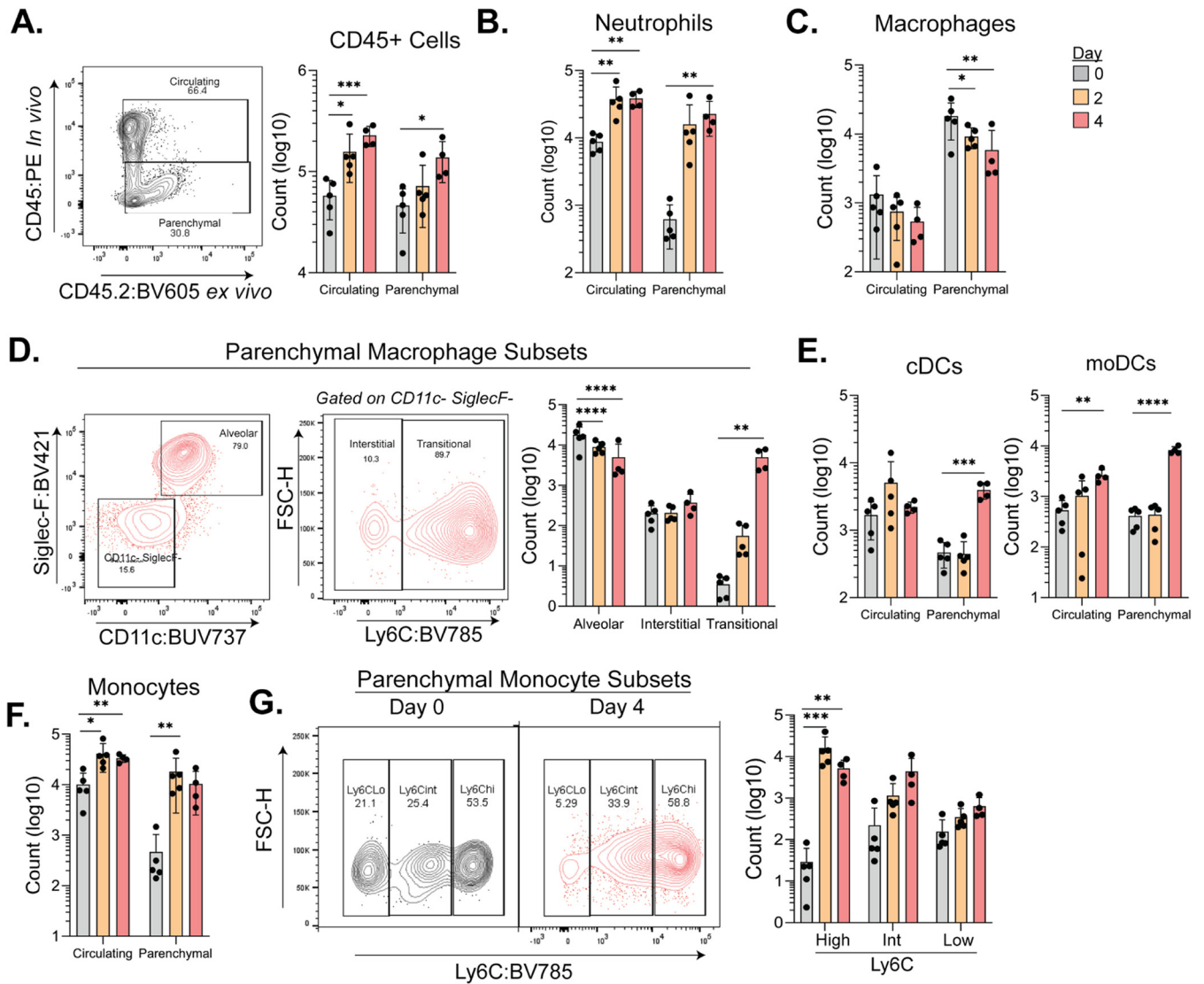
(Continued on next page)

FIG 3 Monocytes and monocyte-derived cells rapidly infiltrate the lung parenchyma in response to MA-SARS-CoV-2 infection. C57BL/6 mice were infected with MA-SARS-CoV-2, and lung tissue was harvested at 0, 2, and 4 days p.i. and analyzed via flow cytometry. (A) Five minutes prior to euthanization, mice were intravitally labeled with CD45:PE. Representative gating of *in vivo*-labeled CD45$^+$ cells used to identify lung circulating (CD45$^+$ *in vivo*) or lung parenchymal (CD45$^-$ *in vivo*) cells is shown. The total number of CD45$^-$ *ex vivo* cells is quantified on the right. (B) Counts of neutrophils (lineage negative CD11b$^+$ Ly6G$^+$) over the course of infection. (C) Counts of macrophages at days 0, 2, and 4 p.i. (lineage negative Ly6G$^-$ CD64$^+$ F4/80$^+$). (D) Representative flow gating for alveolar (Siglec-F$^+$ CD11c$^+$), interstitial (Siglec-F$^-$ CD11c$^-$ Ly6C$^-$), or transitional (Siglec-F$^-$ CD11c$^-$ Ly6C$^+$) macrophages from day 4 p.i. Quantified on the right are the counts of each population. (E) Quantification of cDCs (lineage negative Ly6G$^-$ CD64$^-$ MHC-II$^+$ CD11c$^+$ CD26$^+$) or moDCs (lineage negative Ly6G$^-$ MHC-II$^+$ CD11b$^+$ CD11c$^+$) at the indicated time points. (F) Total monocyte (lineage negative Ly6G$^-$ MHC-II$^-$ CD11c$^-$ CD64 low) counts for circulating or lung parenchymal cells at days 0, 2, and 4 p.i. (G) Representative gating strategy demonstrating forward-scatter height (FSC-H) against Ly6C to identify different monocyte subsets (Ly6C high, Ly6C intermediate [Int], and Ly6C low), with quantification on the right. Results are representative of data from two independent experiments with 5 mice per group. Statistical significance was determined using unpaired one- or two-way ANOVA. *, $P < 0.05$; **, $P < 0.01$; ***, $P < 0.001$; ****, $P < 0.0001$.

We next examined the role of dendritic cells during MA-SARS-CoV-2 infection. Plasmacytoid dendritic cell (pDC) numbers did not change in the circulation or parenchyma at 2 to 4 days p.i. (Fig. S3D). Conventional dendritic cell (cDC) populations remained steady in circulation but increased 10-fold in the lung parenchyma at day 4 p.i.,

FIG 2 Legend (Continued)
scRNA-Seq ($n = 4$ per group). (A) UMAP plot illustrating the different cellular subsets identified in the lung. (B) UMAP distribution of cells from mock- or MA-SARS-CoV-2-infected mice. On the right is the frequency of mock versus infected cells that make up each subset defined by UMAP analysis. (C) Feature plots displaying average expression in normalized read count (NRC) of the indicated gene from mock and infected lungs. (D) GSEA of inflammatory monocytes using the hallmark database from MSigDB for the indicated gene set. (E) Heat map analysis of top-scoring DEGs in alveolar macrophages from mock- or SARS-CoV-2-infected lungs. (F) GSEA plots of the indicated gene set from Liao et al. (6) in alveolar macrophages from mock and infected lungs.

which was primarily due to an increase in cDC type 2 cells (cDC2s) (Fig. 3E; Fig. S3E). Lung parenchymal cDCs increased the expression of MHC-I and CD86 in response to MA-SARS-CoV-2 at day 4 p.i. (Fig. S3F). moDCs had slightly increased numbers in circulation and a 10-fold increase in lung parenchymal populations at day 4 p.i. (Fig. 3E). Parenchymal moDCs also upregulated the expression of MHC-I and CD86 at day 4 p.i. compared to uninfected controls (Fig. S3G). Thus, cDCs and moDCs undergo expansion and activation in response to MA-SARS-CoV-2 infection in the lung.

Investigation of monocyte dynamics during MA-SARS-CoV-2 infection showed a 5-fold increase in circulating monocytes and a 20-fold increase in lung parenchymal monocytes by day 2 p.i. that remained high through day 4 p.i. (Fig. 3F). Ly6C-high monocytes drove monocytic infiltration into the lung, as their numbers increased 100-fold at days 2 and 4 p.i., but the numbers of Ly6C-low monocytes remained constant (Fig. 3G). All lung parenchymal monocytes showed increased expression of MHC-I at day 4 p.i. (Fig. S3H). Ly6C-high monocytes had particularly elevated expression of CD86 (2,000% increase) at day 4 p.i. compared to mock (Fig. S3I). Analysis of splenic immunity found that neutrophils had significantly increased numbers at day 4 p.i. (Fig. S4A). Dendritic cells showed increased expression of MHC-I at 4 days p.i. (Fig. S4B). Together, these data show that MA-SARS-CoV-2 infection prompts systemic immune activation and a lung parenchymal immune response dominated by the infiltration of activated monocytes and monocyte-derived cells.

Expansion of monocyte-derived cells in the lung parenchyma during MA-SARS-CoV-2 infection is CCR2 dependent. Classical Ly6C-high monocytes migrate to the lung parenchyma in a CCR2-dependent manner and can differentiate into interstitial macrophages or moDCs (11, 19). Additionally, we observed high expression levels of CCR2 ligands (*Ccl2*) (Fig. 1F and Fig. 2C) and CCR2 on lung-infiltrating monocytes (Fig. 2C). Therefore, we next evaluated the contribution of CCR2 signaling to the recruitment of monocytes to the lung during MA-SARS-CoV-2 infection. Flow cytometry analysis of lungs at day 4 p.i. found similar circulating monocyte numbers but a 2-fold drop in the number of lung parenchyma-infiltrating monocytes in *Ccr2*$^{-/-}$ mice compared to the wild type (WT) (Fig. 4A). This decrease appeared to be driven by a 4-fold drop in Ly6C-high and Ly6C-intermediate monocytes in the lungs of *Ccr2*$^{-/-}$ mice (Fig. 4B). Circulating moDC numbers were unaltered by the absence of CCR2, but lung parenchymal moDCs dropped 10-fold in *Ccr2*$^{-/-}$ mice at day 4 p.i. (Fig. 4C). cDC numbers in circulation were similar between WT and *Ccr2*$^{-/-}$ mice at day 4 p.i., but lung parenchymal cDC numbers at day 4 p.i. were 5-fold lower than those of the WT (Fig. 4D). This was due to a specific loss of cDC2s (Fig. 4D). All monocyte subsets showed decreased expression of CD86 (2-fold decrease) at day 4 p.i. in *Ccr2*$^{-/-}$ mice, while MHC-I levels were decreased only in the Ly6C-intermediate subset (Fig. 4E). The expression of antigen presentation markers on moDCs was unchanged by CCR2 (Fig. S5A). Lung-infiltrating cDC2s from *Ccr2*$^{-/-}$ mice had lower expression levels of MHC-I, but not CD86, than WT cells at 4 days p.i. (Fig. S5B). Together, these data show that CCR2 signaling promotes the infiltration of activated Ly6C-high and -intermediate monocytes, moDCs, and cDC2s into the lung parenchyma during MA-SARS-CoV-2 infection.

We investigated if CCR2-low/negative innate immune cells (Fig. 3C) were impacted by secondary effects of CCR2. The total number of macrophages in circulation or in the lung parenchyma was not affected by CCR2 4 days after infection with MA-SARS-CoV-2 (Fig. 4F). Alveolar and interstitial macrophages were not impacted by CCR2 signaling. However, *Ccr2*$^{-/-}$ mice had a 10-fold drop in transitional macrophage numbers compared to WT mice (Fig. 4G). The expression of CD86 and MHC-I was also decreased on transitional macrophages from *Ccr2*$^{-/-}$ mice at day 4 p.i. Despite similar numbers in WT and *Ccr2*$^{-/-}$ mice, interstitial macrophages failed to upregulate the expression of both MHC-I and CD86 in *Ccr2*$^{-/-}$ mice at day 4 p.i. The mean fluorescence intensity (MFI) of the expression of CD86 on alveolar macrophages from *Ccr2*$^{-/-}$ mice was modestly decreased compared to the WT (Fig. 4H). Thus, the activation of macrophages and expansion of transitional macrophages are CCR2 dependent during MA-SARS-CoV-2 infection.

Lung parenchymal granulocyte numbers were not significantly altered between WT and *Ccr2*$^{-/-}$ mice at day 4 p.i. (Fig. S5C). However, there was a modest increase in the
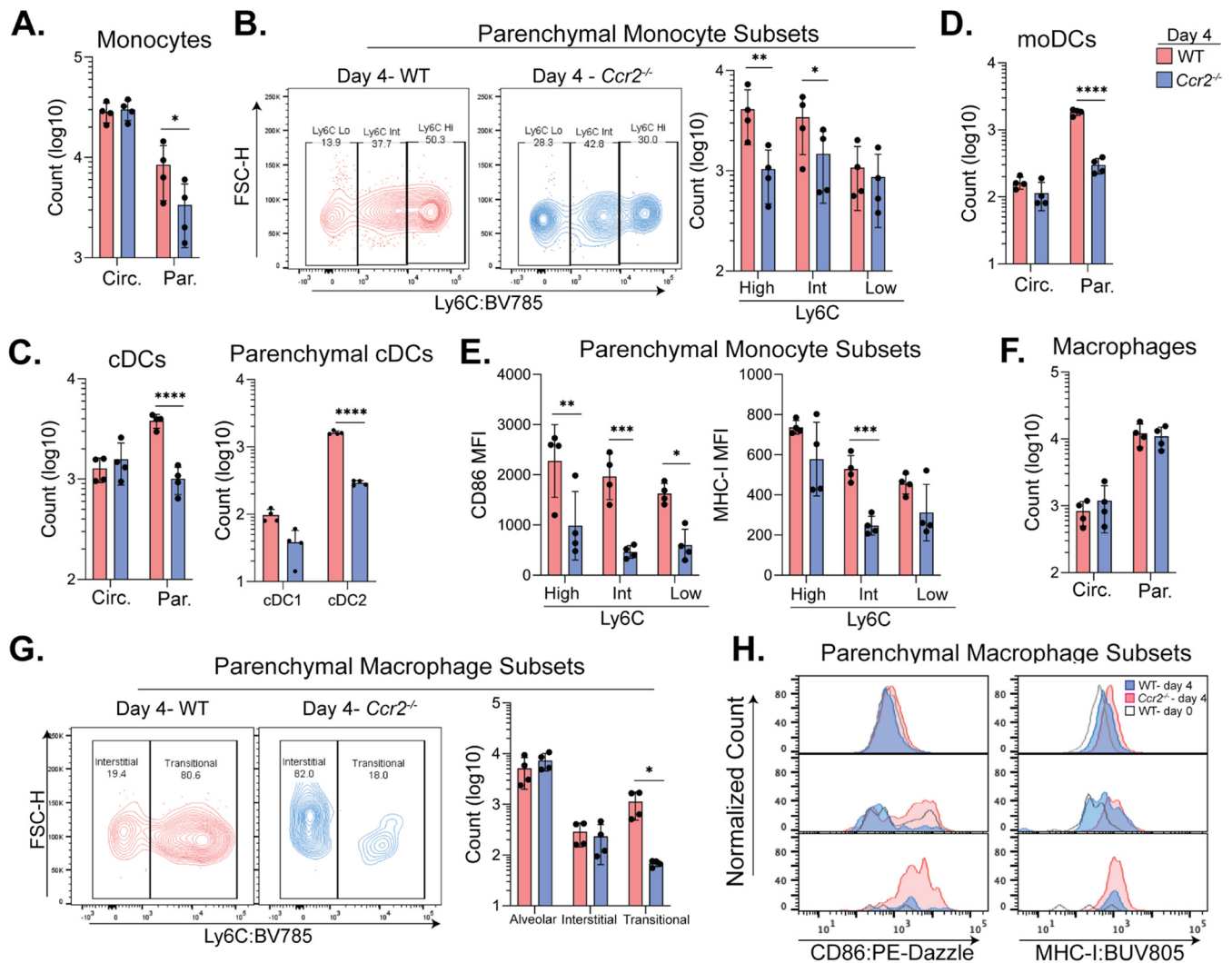
FIG 4 Expansion of monocyte-derived cells in the lung during MA-SARS-CoV-2 infection is CCR2 dependent. C57BL/6 and $Ccr2^{-/-}$ mice were infected with MA-SARS-CoV-2, and lung tissue was harvested at 0 and 4 days p.i. and analyzed via flow cytometry. Circulating (Circ.) versus parenchymal (Par.) cells were distinguished as described in the legend of Fig. 2. (A) Number of total monocytes in the lung circulation or parenchyma. (B) Representative gating identifying Ly6C-high, -intermediate (Int), or -low monocytes from WT and $Ccr2^{-/-}$ lung parenchyma. Counts for each subset are quantified to the right. (C) Quantification of moDCs at day 4 p.i. (D) Total numbers of cDCs and parenchymal cDC subsets (right). (E) MFIs for CD86 (left) and MHC-I (right) expression on monocyte subsets from the lung parenchyma. (F) Quantification of the total macrophage numbers at day 4 p.i. (G) Representative flow plots illustrating interstitial or transitional macrophage populations from WT and $Ccr2^{-/-}$ lung-infiltrating cells. Counts of macrophage subsets are quantified on the right. (H) Representative histograms of the MFIs for CD86 (left) and MHC-I (right) for each macrophage subset at 4 days p.i. from WT, $Ccr2^{-/-}$, or WT mock lung-infiltrating cells. Results are representative of data from two independent experiments with 5 mice per group. Statistical significance was determined using unpaired one- or two-way ANOVA. *, $P < 0.05$; **, $P < 0.01$; ***, $P < 0.001$; ****, $P < 0.0001$.

number of granulocytes in circulation and the spleen from $Ccr2^{-/-}$ mice compared to WT mice at day 4 p.i. (Fig. S5C and D). Total splenic macrophage numbers were also higher in the absence of CCR2 at day 4 p.i. (Fig. S5D). Monocyte, moDC, and pDC populations in the spleen were unaffected by CCR2; however, numbers of cDCs in the spleen were increased in $Ccr2^{-/-}$ mice at day 4 p.i. compared to the WT (Fig. S5D). These data identify a role for CCR2 in promoting the infiltration of activated, Ly6C-high monocytes and monocyte-derived cells to the lung during MA-SARS-CoV-2 infection.

CCR2 signaling restricts SARS-CoV-2 in the lung. To determine if CCR2 was protective against MA-SARS-CoV-2, we infected WT or $Ccr2^{-/-}$ mice with MA-SARS-CoV-2 and assessed the viral burden at day 4 p.i. $Ccr2^{-/-}$ mice had a 10-fold-higher viral burden in lung tissue as measured by a plaque assay or qRT-PCR (Fig. 5A and B). At day 4 p.i., $Ifnl2$, cytokines ($Il6$), and chemokines ($Cxcl10$ and $Ccl2$) were elevated in $Ccr2^{-/-}$ compared to WT lungs (Fig. 5C). $In\ situ$ hybridization showed that $Ccr2^{-/-}$ lungs had
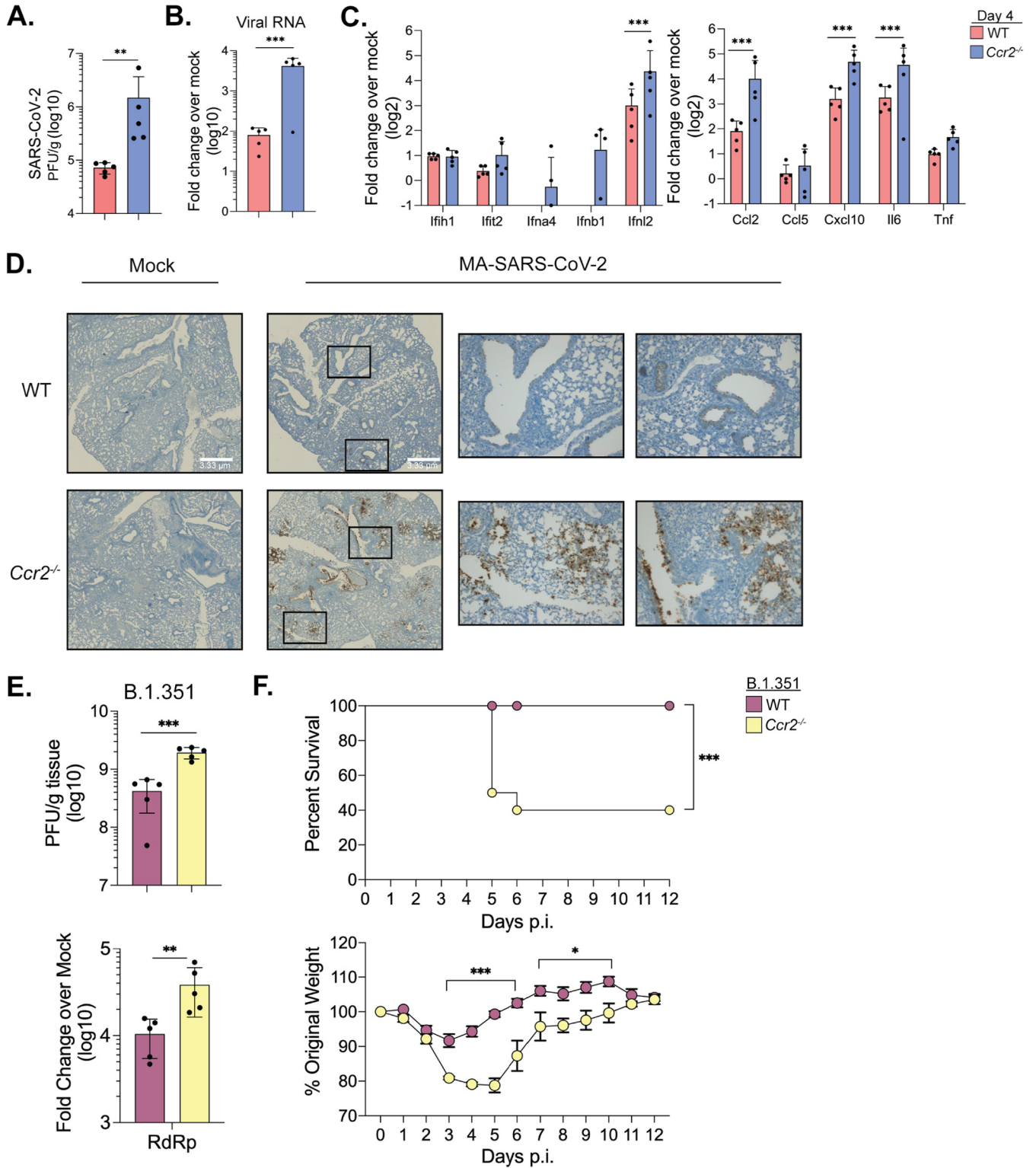
FIG 5 CCR2 restricts MA-SARS-CoV-2 burden and inflammatory cytokines in the lung. C57BL/6 or $Ccr2^{-/-}$ mice were infected with MA-SARS-CoV-2, and lung tissue was collected at day 4 p.i. (A) Infectious virus at day 4 p.i. as quantified via plaque assays. (B) qRT-PCR for SARS-CoV-2 RdRp. (C) qRT-PCR was performed to probe for the indicated IFN signaling (left) or inflammatory (right) transcripts. (D) Representative images of *in situ* hybridization to visualize MA-SARS-CoV-2 RNA in lung tissue slices from 0 and 4 days p.i. in both WT and $Ccr2^{-/-}$ mice. (E) WT or $Ccr2^{-/-}$ mice were infected with B.1.351, and lungs were harvested at day 4 p.i. Virus was quantified via a plaque assay (top) or qRT-PCR (bottom). (F) WT and $Ccr2^{-/-}$ mice were monitored over 12 days after infection with B.1.351 for survival (top) and weight loss (bottom). Results are representative of data from two independent experiments with 5 mice per group. Statistical significance was determined using unpaired Student's t test, one-way ANOVA, or Kaplan-Meier survival curve analysis. *, $P < 0.05$; **, $P < 0.01$; ***, $P < 0.001$; ****, $P < 0.0001$.

more robust detection of viral RNA than WT mice. Additionally, while viral RNA was localized to cells lining the airway spaces in WT mice, $Ccr2^{-/-}$ lungs had infiltration of viral RNA further into the interstitial and parenchymal spaces (Fig. 5D). Next, we investigated if CCR2 restricted B.1.351 infection. $Ccr2^{-/-}$ mice had a significantly higher viral burden in the lung at day 4 p.i. than did WT mice, as assessed by a plaque assay or qRT-PCR (Fig. 5E). To determine the impact of a higher viral burden on SARS-CoV-2 infection outcomes, we performed a survival study of WT and $Ccr2^{-/-}$ mice using B.1.351. $Ccr2^{-/-}$ mice lost 10% more weight than their WT counterparts. While infection with B.1.351 did not cause mortality in WT mice, B.1.351 infection resulted in 60% mortality in $Ccr2^{-/-}$ mice (Fig. 5F). Together, these data show that CCR2-mediated signaling and immune cell recruitment restrict inflammation, viral burden, and viral dissemination in the lung to provide protection against SARS-CoV-2 infection.

DISCUSSION

SARS-CoV-2 infection in humans has identified a robust and reproducible correlation between inflammatory cytokine levels and disease severity during COVID-19 (6). In accordance, we found that SARS-CoV-2-infected mice had a proinflammatory cytokine profile in the lung containing pyrogens (*Il6* and *Tnf*), chemoattractants for monocytes (*Ccl2*) and T cells (*Cxcl10*), ISGs (*Irf7* and *Isg15*), alarmins (*S100a8*), and matrix metalloproteinases (*Mmp14*) (6, 20–23). Interestingly, inflammatory gene expression in the lung was MA-SARS-CoV-2 viral load dependent, as most cytokine transcripts surveyed by quantitative PCR (qPCR) positively correlated with viral RNA. Similar phenomena have been noted in human subjects, with one study describing an association between SARS-CoV-2 burden, IL-6 levels, and an increased risk of death (24). Similar to studies of postmortem lung tissue or BAL fluids from patients suffering from COVID-19, we observed a significant increase in the numbers of $S100a8^+$ granulocytes in the lung parenchyma (4, 6–8). S100a8/9 and Toll-like receptor 4 (TLR4) signaling mediate the emergence of a dysregulated neutrophil population that promotes SARS-CoV-2 disease (18). Neutrophil and inflammatory cytokine levels were higher in $Ccr2^{-/-}$ mice, likely driven by the increased viral burden in $Ccr2^{-/-}$ lungs. Thus, the MA-SARS-CoV-2 burden is likely directly driving cytokine expression and neutrophilic infiltration into the lung.

CCR2 expression is a defining feature of inflammatory Ly6C-high blood monocytes (9). In various models of respiratory disease, including influenza, *Mycobacterium tuberculosis*, and allergic inflammation, deletion of *Ccr2* negates the ability of monocytes to enter the lung parenchyma (11, 25, 26). Similarly, we found that CCR2 had no effect on circulating monocyte numbers but specifically promoted the infiltration of activated monocytes into the lung parenchyma during SARS-CoV-2 infection. However, unlike in influenza, $Ccr2^{-/-}$ mice still had a significant increase in lung-infiltrating Ly6C-high monocytes compared to mock, suggesting that CCR2 signaling may be partially redundant during SARS-CoV-2 infection (11). Inflammatory monocytes express a variety of chemokine receptors, including CXCR3, whose ligand (CXCL10) is elevated in $Ccr2^{-/-}$ mice and could compensate for the loss of CCR2. Monocyte-derived interstitial macrophages and moDCs also depended on CCR2 for expansion in the lung parenchyma (27). In contrast, alveolar macrophages, which are self-renewing and primarily fetus derived, were unaffected by the absence of CCR2 (28–30). Previous studies in a model of sterile lung inflammation demonstrated that DC precursors required CCR2 for entry into the lung, and accordingly, in MA-SARS-CoV-2 infection, cDC2 lung parenchymal populations were also decreased in the absence of CCR2 (31). These data suggest that CCR2 plays an essential and specific role in promoting the recruitment and differentiation of monocytes into transitional macrophage and moDC populations during MA-SARS-CoV-2 infection. In this study, we focused on the role of monocyte-derived cells; however, CCR2 is expressed on other cell populations, including NK cells and T cells. Exploration of CCR2 signaling on other cell types at early and late time points will be an important topic for future studies to explore the role of CCR2 signaling in both innate and adaptive responses.

In contrast to other respiratory infections such as influenza, in which CCR2 promotes mortality and inflammation, our study found that CCR2 restricted viral burden and weight loss during MA-SARS-CoV-2 infection (11). CCR2 promoted the infiltration of monocyte-derived cells into the lung parenchyma, and while we did not directly assess the role of monocytes in restricting virus, this suggests an essential role for Ly6C-high monocytes, moDCs, and transitional macrophages in controlling SARS-CoV-2 infection. Macrophages were previously shown to control viruses through the secretion of inducible nitric oxide synthase (iNOS) and the phagocytosis of viral particles, while moDCs play a key role in type I IFN release and priming the T cell response (13, 32). Further studies are needed to delineate the precise mechanisms that these cell subsets use to control SARS-CoV-2. Current evidence in the field of SARS-CoV-2 research suggests that a large portion of the pathology of COVID-19 is due to a monocyte-driven cytokine storm (33). Here, we identify data that suggest that monocyte-derived cells in the lung are crucial for limiting viral burden and cytokine production during the early stages of MA-SARS-CoV-2 infection. Most studies to date of the immune response in humans have focused on late time points of infection; therefore, monocytes could be protective early and pathological later during infection resolution. The consideration of the role of monocyte-derived cells in restricting SARS-CoV-2 infection in the lung and priming adaptive immune responses will be essential for the design of future therapies and vaccines.

MATERIALS AND METHODS

Viruses and cells. VeroE6 cells were obtained from the ATCC (clone E6; ATCC CRL-1586) and cultured in complete Dulbecco's modified Eagle's medium (DMEM) consisting of $1\times$ DMEM (catalog number 45000-304; VWR), 10% fetal bovine serum (FBS), 25 mM HEPES buffer (Corning Cellgro), 2 mM L-glutamine, 1 mM sodium pyruvate, $1\times$ nonessential amino acids, and $1\times$ antibiotics. VeroE6-TMPRSS2-hACE2 cells were kindly provided by Barney Graham (Vaccine Research Center, NIH, Bethesda, MD). The generation of MA-SARS-CoV-2 will be described in a future publication. In brief, MA-SARS-CoV-2 was generated by engineering four coding mutations (NSP6 L37F, NSP10 P87S, S N501Y, and N D128Y) into the backbone of icSARS-CoV-2 (WA/1 backbone). This virus was then passaged 20 times in BALB/c mice, followed by deep sequencing, which identified 3 additional acquired mutations (S T417N, S H655Y, and E E8V). This virus, termed MA-SARS-CoV-2, was passaged once in VeroE6 cells to generate a working stock. The B.1.351 variant was provided by Andy Pekosz (John Hopkins University, Baltimore, MD). Viral stocks were grown on VeroE6 cells, and viral titers were determined by plaque assays on VeroE6 cells or VeroE6-TMPRSS2-hACE2 cells (ATCC). Vero cells were cultured in complete DMEM consisting of $1\times$ DMEM (Corning Cellgro), 10% FBS, 25 mM HEPES buffer (Corning Cellgro), 2 mM L-glutamine, 1 mM sodium pyruvate, $1\times$ nonessential amino acids, and $1\times$ antibiotics. VeroE6-TMPRSS2-hACE2 cells were cultured in complete DMEM in the presence of puromycin at 10 mg/ml (catalog number A11138-03; Gibco).

Infection of mice with MA-SARS-CoV-2. C57BL/6J and $Ccr2^{-/-}$ mice were purchased from Jackson Laboratories or bred in-house at the Yerkes National Primate Research Center rodent facility at Emory University. All mice used in these experiments were females between 8 and 12 weeks of age. Stock MA-SARS-CoV-2 or B.1.351 virus was diluted in phosphate-buffered saline (PBS) to a working concentration of 1×10^7 PFU/ml. Mice were anesthetized with isoflurane and infected intranasally with virus (50 μl; 5×10^5 PFU/mouse) in an animal biosafety level 3 (ABSL-3) facility. Mice were monitored daily for weight loss. All experiments adhered to the guidelines approved by the Emory University Institutional Animal Care and Use Committee.

Quantification of infectious virus. At the indicated day postinfection, mice were euthanized via isoflurane overdose, and lung tissue was collected in Omni-Bead Ruptor tubes filled with 1% FBS–Hanks' balanced salt solution (HBSS). Tissue was homogenized in an Omni Bead Ruptor 24 instrument (5.15 ms, 15 s). To perform plaque assays, 10-fold dilutions of the viral supernatant in serum-free DMEM (catalog number 45000-304; VWR) were overlaid onto VeroE6-TMPRSS2-hACE2 cells monolayers and adsorbed for 1 h at 37°C. After adsorption, 0.5% immunodiffusion agarose in $2\times$ DMEM supplemented with 5% FBS (Atlanta Biologics) and $1\times$ sodium bicarbonate was overlaid, and cultures were incubated for 48 h at 37°C. Agarose plugs were removed, cells were fixed with 4% PBS-buffered paraformaldehyde (PFA) for 15 min at room temperature, and plaques were visualized using crystal violet staining (20% methanol in double-distilled water [ddH$_2$O]).

Quantitative reverse transcription-PCR of lung tissues. At the indicated day postinfection, mice were euthanized with an isoflurane overdose, and one lobe of lung tissue was collected in an Omni Bead Ruptor tube filled with Tri reagent (catalog number R2050-1-200; Zymo). Tissue was homogenized using an Omni Bead Ruptor 24 instrument (5.15 ms, 15 s) and then centrifuged to remove debris. RNA was extracted using a Direct-zol RNA miniprep kit (catalog number R2051; Zymo) and then converted to cDNA using a high-capacity reverse transcriptase cDNA kit (catalog number 4368813; Thermo). RNA levels were quantified using the IDT Prime Time gene expression master mix and TaqMan gene expression primer/probe sets (IDT). All qPCRs were performed in 384-well plates and run on a QuantStudio5 qPCR system. SARS-CoV-2 RNA-dependent RNA polymerase levels were measured as previously described (5). The following TaqMan primer/probe sets (Thermo Fisher) were used in this study: *Gapdh* (Mm99999915_g1),

Ifnl2 (Mm04204155_gH), *Ifit2* (Mm00492606_m1), *Ifih1* (Mm00459183_m1), *Ifnb1* (Mm00439552_s1), *Ifna4* (Mm00833969_s1), *Ccl2* (Mm00441242_m1), *Ccl5* (Mm01302427_m1), *Cxcl10* (Mm99999072_m1), *Tnf* (Mm00443258_m1), *Il1b* (Mm00434228_m1), and *Il6* (Mm00446190_m1).

Processing of mouse tissues to single-cell suspensions. At the indicated day postinfection, mice were anesthetized using isoflurane and injected retro-orbitally with CD45:PE (100 μl per mouse, diluted 1:20 in PBS). Mice were allowed to recover for 5 min and then euthanized via an isoflurane overdose. One lobe of lung tissue and spleens were collected from each mouse and placed into 1% FBS–HBSS. Spleens were mechanically homogenized on a 70-μm cell strainer, and the cell suspension was collected in 10% FBS–RPMI 1640. The splenocyte suspension was spun down (1,250 rpm for 5 min at 4°C) and lysed in ACK lysis buffer (Lonza) for 5 min on ice. Splenocytes were washed with 10% FBS–RPMI 1640 and then kept on ice until ready for downstream applications. Lungs were mechanically disrupted in 6-well plates and then digested for 30 min at 37°C in a solution of DNase I (2,000 U/ml) (catalog number D4527-500KU; Sigma) and collagenase (5 mg/ml) (catalog number 11088882001; Sigma) in HBSS. Digestion was stopped with 10% FBS–RPMI 1640, and lungs were pushed through a 70-μm filter to obtain a single-cell suspension. Cells were resuspended in 30% Percoll–PBS and centrifuged at 2,000 rpm for 20 min. The top layer of cell debris was removed, and the cell pellet at the bottom was lysed with ACK lysis buffer for 5 min on ice. Cells were washed, resuspended in 10% FBS–RPMI 1640, and kept on ice until ready for staining.

Flow cytometry analysis. Single-cell suspensions were spun down and resuspended in anti-CD16/32 (clone 2.4G2; Tonbo) blocking solution for 20 min at 4°C. Cell suspensions were spun down and stained with Live/Dead Ghost dye stain (Tonbo Biosciences) for 20 min at 4°C. Cells were washed and resuspended in the indicated surface stain in fluorescence-activated cell sorter (FACS) buffer for 20 min at 4°C. After staining, cells were washed and fixed in 2% PFA–PBS for 20 min at room temperature. Precision count beads (BioLegend) were added to samples to obtain counts. Samples were run on a BD FACS Symphony A5 system. The following antibodies were used in this study: CD45:PE (clone 30-F11; BioLegend), CD45.2:BV605 (clone 104; BioLegend), CD11b:BUV395 (clone 440c; BD Biosciences), I-A/I-E:AF700 (clone M5/114.15.2; BioLegend), CD11c:BUV737 (clone N418; BioLegend), CD26:PE-Cy7 (clone H194-112; BioLegend), CD172a: BV510 (clone P84; BioLegend), XCR1:AF647 (clone Zet; BioLegend), CD64:peridinin chlorophyll protein-Cy5.5 (PerCpCy5.5) (clone X54-5/7.1; BioLegend), F4/80:fluorescein isothiocyanate (FITC) (clone BM8; BioLegend), H2kb:BUV805 (clone AF6-88.5; BD Biosciences), CD86:PE-Dazzle594 (clone GL1; BioLegend), Live/Dead Ghost dye:R780 (Tonbo), CD3:allophycocyanin (APC)-Cy7 (clone 145-2C11; BioLegend), CD19:APC-Cy7 (clone 1D3; BD Biosciences), NK1.1 (clone PK136; BioLegend), Ly6C:BV785 (clone Hk1.4; BioLegend), Ly6G: BV650 (clone 1A8; BioLegend), and Siglec-F:BV421 (clone E50-2440; BD Biosciences).

***In situ* hybridization of lung tissues.** One lobe of the lung was harvested from mice at 0 or 4 days p.i. and fixed with 4% PFA–PBS for a minimum of 3 days. Formalin-fixed paraffin-embedded lung tissues were deparaffinized through sequential washes twice each in xylene and 100% ethanol for 5 min. Tissues were then pretreated with RNAscope hydrogen peroxide for 10 min at room temperature (RT) and then with RNAscope target retrieval for 5 min at 95°C to 100°C, followed by RNAscope protease plus for 30 min at 40°C. RNA-ISH was performed using a probe against the S gene of SARS-CoV-2 (V-nCoV-2019-S; ACD) using the RNAscope 2.5 HD assay—brown according to the manufacturer's instructions. Slides were coverslipped with ProLong gold antifade mountant (Thermo Fisher). Images were acquired using a Zeiss AxioImager Z2 system with Zeiss software.

Single-cell RNA-Seq analysis. Lungs from mice at 0 or 4 days p.i. were processed to single-cell suspensions as described above. Single-cell suspensions were washed 4 times with PBS and passed through a 70-μm filter. Cell suspensions were counted and captured in droplets using chromium NextGEM single-cell 5′ library and gel bead kits on a 10× chromium controller in a BSL-3 cabinet. Amplification of cDNA and library preparation were performed according to the manufacturer's instructions. Gene expression libraries were sequenced as paired-end 26-by-91 reads on an Illumina NovaSeq6000 system targeting a depth of 50,000 reads per cell at the Yerkes Genomics Core Laboratory (http://www.yerkes.emory.edu/nhp_genomics_core/). Analysis was conducted using R (v4) and Seurat (v4). Cell Ranger (v6) was used for demultiplexing, aligning barcodes, mapping to the genome (mm10), and quantifying UMIs (unique molecular identifiers). Filtered Cell Ranger matrices were processed with the Read10x function in Seurat for preprocessing and cluster analysis. Data were filtered to remove cells with <200 genes, abnormally high gene counts (feature counts of >5,000), and >5% mitochondrial genes. After qualify control, there were 9,399 mock cells and 10,982 CoV-2 cells. Principal-component analysis (PCA) and dimensional reduction were conducted on log-normalized and scaled gene expression data. Clustering was conducted using the FindNeighbors and FindClusters functions, with resolution parameters between 0.5 and 1.4. Overall, 23 clusters were identified, and the FindAllMarkers function was utilized to identify DEGs, from which marker genes for cluster cell annotation was conducted. After annotating cells, DEGs were determined based on subclusters or experimental groups. Gene set enrichment analysis (GSEA) was conducted using the ranked gene list produced with the Seurat FindMarkers function (comparing CoV-2 samples with mock samples), and Genelists were obtained from MsigDB (hallmarks) and data reported previously by Wauters et al. (see the supplemental material in reference 34) (macrophage suppressive and hyperinflammatory). GSEA was conducted using Broad (4.0.3) and plotted in R.

Statistical analysis. All experiments in mice were repeated twice with sample sizes of 4 to 6 for flow cytometry or viral titer experiments and sample sizes of 10 for survival studies. Statistical analysis was performed in GraphPad Prism v8 using the appropriate test for the indicated analysis. The following statistical tests were used in this study: Student's *t* test and unpaired one- or two-way analysis of variance (ANOVA). scRNA-Seq statistical analysis was performed using the programs described above. Throughout the manuscript, a result was not considered significant unless it achieved a *P* value of <0.05.

Data availability. Single-cell RNA sequencing data are publicly accessible through the Gene Expression Omnibus under accession number GSE186360.

SUPPLEMENTAL MATERIAL

Supplemental material is available online only.

FIG S1, TIF file, 0.6 MB.
FIG S2, TIF file, 1.4 MB.
FIG S3, TIF file, 1.4 MB.
FIG S4, TIF file, 0.7 MB.
FIG S5, TIF file, 0.8 MB.

REFERENCES

1. Zhou P, Yang X-L, Wang X-G, Hu B, Zhang L, Zhang W, Si H-R, Zhu Y, Li B, Huang C-L, Chen H-D, Chen J, Luo Y, Guo H, Jiang R-D, Liu M-Q, Chen Y, Shen X-R, Wang X, Zheng X-S, Zhao K, Chen Q-J, Deng F, Liu L-L, Yan B, Zhan F-X, Wang Y-Y, Xiao G-F, Shi Z-L. 2020. A pneumonia outbreak associated with a new coronavirus of probable bat origin. Nature 579:270–273. https://doi.org/10.1038/s41586-020-2012-7.
2. Zhu N, Zhang D, Wang W, Li X, Yang B, Song J, Zhao X, Huang B, Shi W, Lu R, Niu P, Zhan F, Ma X, Wang D, Xu W, Wu G, Gao GF, Tan W, China Novel Coronavirus Investigating and Research Team. 2020. A novel coronavirus from patients with pneumonia in China, 2019. N Engl J Med 382:727–733. https://doi.org/10.1056/NEJMoa2001017.
3. Yin X, Riva L, Pu Y, Martin-Sancho L, Kanamune J, Yamamoto Y, Sakai K, Gotoh S, Miorin L, De Jesus PD, Yang C-C, Herbert KM, Yoh S, Hultquist JF, García-Sastre A, Chanda SK. 2021. MDA5 governs the innate immune response to SARS-CoV-2 in lung epithelial cells. Cell Rep 34:108628. https://doi.org/10.1016/j.celrep.2020.108628.
4. Arunachalam PS, Wimmers F, Mok CKP, Perera RAPM, Scott M, Hagan T, Sigal N, Feng Y, Bristow L, Tak-Yin Tsang O, Wagh D, Coller J, Pellegrini KL, Kazmin D, Alaaeddine G, Leung WS, Chan JMC, Chik TSH, Choi CYC, Huerta C, Paine McCullough M, Lv H, Anderson E, Edupuganti S, Upadhyay AA, Bosinger SE, Maecker HT, Khatri P, Rouphael N, Peiris M, Pulendran B. 2020. Systems biological assessment of immunity to mild versus severe COVID-19 infection in humans. Science 369:1210–1220. https://doi.org/10.1126/science.abc6261.
5. Vanderheiden A, Ralfs P, Chirkova T, Upadhyay AA, Zimmerman MG, Bedoya S, Aoued H, Tharp GM, Pellegrini KL, Manfredi C, Sorscher E, Mainou B, Lobby JL, Kohlmeier JE, Lowen AC, Shi P-Y, Menachery VD, Anderson LJ, Grakoui A, Bosinger SE, Suthar MS. 2020. Type I and type III interferons restrict SARS-CoV-2 infection of human airway epithelial cultures. J Virol 94: e00985-20. https://doi.org/10.1128/JVI.00985-20.
6. Liao M, Liu Y, Yuan J, Wen Y, Xu G, Zhao J, Cheng L, Li J, Wang X, Wang F, Liu L, Amit I, Zhang S, Zhang Z. 2020. Single-cell landscape of bronchoalveolar immune cells in patients with COVID-19. Nat Med 26: 842–844. https://doi.org/10.1038/s41591-020-0901-9.
7. Wang C, Xie J, Zhao L, Fei X, Zhang H, Tan Y, Nie X, Zhou L, Liu Z, Ren Y, Yuan L, Zhang Y, Zhang J, Liang L, Chen X, Liu X, Wang P, Han X, Weng X, Chen Y, Yu T, Zhang X, Cai J, Chen R, Shi Z-L, Bian X-W. 2020. Alveolar macrophage dysfunction and cytokine storm in the pathogenesis of two severe COVID-19 patients. EBioMedicine 57:102833. https://doi.org/10.1016/j.ebiom.2020.102833.
8. Szabo PA, Dogra P, Gray JI, Wells SB, Connors TJ, Weisberg SP, Krupska I, Matsumoto R, Poon MML, Idzikowski E, Morris SE, Pasin C, Yates AJ, Ku A, Chait M, Davis-Porada J, Guo XV, Zhou J, Steinle M, Mackay S, Saqi A, Baldwin MR, Sims PA, Farber DL. 2021. Longitudinal profiling of respiratory and systemic immune responses reveals myeloid cell-driven lung inflammation in severe COVID-19. Immunity 54:797–814.e6. https://doi.org/10.1016/j.immuni.2021.03.005.
9. Geissmann F, Jung S, Littman DR. 2003. Blood monocytes consist of two principal subsets with distinct migratory properties. Immunity 19:71–82. https://doi.org/10.1016/S1074-7613(03)00174-2.
10. Srivastava M, Jung S, Wilhelm J, Fink L, Bühling F, Welte T, Bohle RM, Seeger W, Lohmeyer J, Maus UA. 2005. The inflammatory versus constitutive trafficking of mononuclear phagocytes into the alveolar space of mice is associated with drastic changes in their gene expression profiles. J Immunol 175:1884–1893. https://doi.org/10.4049/jimmunol.175.3.1884.
11. Lin KL, Suzuki Y, Nakano H, Ramsburg E, Gunn MD. 2008. CCR2+ monocyte-derived dendritic cells and exudate macrophages produce influenza-induced pulmonary immune pathology and mortality. J Immunol 180:2562–2572. https://doi.org/10.4049/jimmunol.180.4.2562.
12. Seo S-U, Kwon H-J, Ko H-J, Byun Y-H, Seong BL, Uematsu S, Akira S, Kweon M-N. 2011. Type I interferon signaling regulates Ly6C(hi) monocytes and neutrophils during acute viral pneumonia in mice. PLoS Pathog 7:e1001304. https://doi.org/10.1371/journal.ppat.1001304.

13. Cao W, Taylor AK, Biber RE, Davis WG, Kim JH, Reber AJ, Chirkova T, De La Cruz JA, Pandey A, Ranjan P, Katz JM, Gangappa S, Sambhara S. 2012. Rapid differentiation of monocytes into type I IFN-producing myeloid dendritic cells as an antiviral strategy against influenza virus infection. J Immunol 189:2257–2265. https://doi.org/10.4049/jimmunol.1200168.

14. Xie X, Muruato A, Lokugamage KG, Narayanan K, Zhang X, Zou J, Liu J, Schindewolf C, Bopp NE, Aguilar PV, Plante KS, Weaver SC, Makino S, LeDuc JW, Menachery VD, Shi P-Y. 2020. An infectious cDNA clone of SARS-CoV-2. Cell Host Microbe 27:841–848.e3. https://doi.org/10.1016/j.chom.2020.04.004.

15. Gu H, Chen Q, Yang G, He L, Fan H, Deng Y-Q, Wang Y, Teng Y, Zhao Z, Cui Y, Li Y, Li X-F, Li J, Zhang N-N, Yang X, Chen S, Guo Y, Zhao G, Wang X, Luo D-Y, Wang H, Yang X, Li Y, Han G, He Y, Zhou X, Geng S, Sheng X, Jiang S, Sun S, Qin C-F, Zhou Y. 2020. Adaptation of SARS-CoV-2 in BALB/c mice for testing vaccine efficacy. Science 369:1603–1607. https://doi.org/10.1126/science.abc4730.

16. Hou YJ, Okuda K, Edwards CE, Martinez DR, Asakura T, Dinnon KH, Kato T, Lee RE, Yount BL, Mascenik TM, Chen G, Olivier KN, Ghio A, Tse LV, Leist SR, Gralinski LE, Schäfer A, Dang H, Gilmore R, Nakano S, Sun L, Fulcher ML, Livraghi-Butrico A, Nicely NI, Cameron M, Cameron C, Kelvin DJ, de Silva A, Margolis DM, Markmann A, Bartelt L, Zumwalt R, Martinez FJ, Salvatore SP, Borczuk A, Tata PR, Sontake V, Kimple A, Jaspers I, O'Neal WK, Randell SH, Boucher RC, Baric RS. 2020. SARS-CoV-2 reverse genetics reveals a variable infection gradient in the respiratory tract. Cell 182:429–446.e14. https://doi.org/10.1016/j.cell.2020.05.042.

17. Tegally H, Wilkinson E, Giovanetti M, Iranzadeh A, Fonseca V, Giandhari J, Doolabh D, Pillay S, San EJ, Msomi N, Mlisana K, von Gottberg A, Walaza S, Allam M, Ismail A, Mohale T, Glass AJ, Engelbrecht S, Van Zyl G, Preiser W, Petruccione F, Sigal A, Hardie D, Marais G, Hsiao N-Y, Korsman S, Davies M-A, Tyers L, Mudau I, York D, Maslo C, Goedhals D, Abrahams S, Laguda-Akingba O, Alisoltani-Dehkordi A, Godzik A, Wibmer CK, Sewell BT, Lourenço J, Alcantara LCJ, Kosakovsky Pond SL, Weaver S, Martin D, Lessells RJ, Bhiman JN, Williamson C, de Oliveira T. 2021. Detection of a SARS-CoV-2 variant of concern in South Africa. Nature 592:438–443. https://doi.org/10.1038/s41586-021-03402-9.

18. Guo Q, Zhao Y, Li J, Liu J, Yang X, Guo X, Kuang M, Xia H, Zhang Z, Cao L, Luo Y, Bao L, Wang X, Wei X, Deng W, Wang N, Chen L, Chen J, Zhu H, Gao R, Qin C, Wang X, You F. 2021. Induction of alarmin S100A8/A9 mediates activation of aberrant neutrophils in the pathogenesis of COVID-19. Cell Host Microbe 29:222–235.e4. https://doi.org/10.1016/j.chom.2020.12.016.

19. Tsou C-L, Peters W, Si Y, Slaymaker S, Aslanian AM, Weisberg SP, Mack M, Charo IF. 2007. Critical roles for CCR2 and MCP-3 in monocyte mobilization from bone marrow and recruitment to inflammatory sites. J Clin Invest 117:902–909. https://doi.org/10.1172/JCI29919.

20. Chua RL, Lukassen S, Trump S, Hennig BP, Wendisch D, Pott F, Debnath O, Thürmann L, Kurth F, Völker MT, Kazmierski J, Timmermann B, Twardziok S, Schneider S, Machleidt F, Müller-Redetzky H, Maier M, Krannich A, Schmidt S, Balzer F, Liebig J, Loske J, Suttorp N, Eils J, Ishaque N, Liebert UG, von Kalle C, Hocke A, Witzenrath M, Goffinet C, Drosten C, Laudi S, Lehmann I, Conrad C, Sander L-E, Eils R. 2020. COVID-19 severity correlates with airway epithelium-immune cell interactions identified by single-cell analysis. Nat Biotechnol 38:970–979. https://doi.org/10.1038/s41587-020-0602-4.

21. Schulte-Schrepping J, Reusch N, Paclik D, Baßler K, Schlickeiser S, Zhang B, Krämer B, Krammer T, Brumhard S, Bonaguro L, De Domenico E, Wendisch D, Grasshoff M, Kapellos TS, Beckstette M, Pecht T, Saglam A, Dietrich O, Mei HE, Schulz AR, Conrad C, Kunkel D, Vafadarnejad E, Xu C-J, Horne A, Herbert M, Drews A, Thibeault C, Pfeiffer M, Hippenstiel S, Hocke A, Müller-Redetzky H, Heim K-M, Machleidt F, Uhrig A, Bosquillon de Jarcy L, Jürgens L, Stegemann M, Glösenkamp CR, Volk H-D, Goffinet C, Landthaler M, Wyler E, Georg P, Schneider M, Dang-Heine C, Neuwinger N, Kappert K, Tauber R, Corman V, et al. 2020. Severe COVID-19 is marked by a dysregulated myeloid cell compartment. Cell 182:1419–1440.e23. https://doi.org/10.1016/j.cell.2020.08.001.

22. Silvin A, Chapuis N, Dunsmore G, Goubet A-G, Dubuisson A, Derosa L, Almire C, Hénon C, Kosmider O, Droin N, Rameau P, Catelain C, Alfaro A, Dussiau C, Friedrich C, Sourdeau E, Marin N, Szwebel T-A, Cantin D, Mouthon L, Borderie D, Deloger M, Bredel D, Mouraud S, Drubay D, Andrieu M, Lhonneur A-S, Saada V, Stoclin A, Willekens C, Pommeret F, Griscelli F, Ng LG, Zhang Z, Bost P, Amit I, Barlesi F, Marabelle A, Pène F, Gachot B, André F,

Zitvogel L, Ginhoux F, Fontenay M, Solary E. 2020. Elevated calprotectin and abnormal myeloid cell subsets discriminate severe from mild COVID-19. Cell 182:1401–1418.e18. https://doi.org/10.1016/j.cell.2020.08.002.

23. Xiong Y, Liu Y, Cao L, Wang D, Guo M, Jiang A, Guo D, Hu W, Yang J, Tang Z, Wu H, Lin Y, Zhang M, Zhang Q, Shi M, Liu Y, Zhou Y, Lan K, Chen Y. 2020. Transcriptomic characteristics of bronchoalveolar lavage fluid and peripheral blood mononuclear cells in COVID-19 patients. Emerg Microbes Infect 9:761–770. https://doi.org/10.1080/22221751.2020.1747363.

24. Fajnzylber J, Regan J, Coxen K, Corry H, Wong C, Rosenthal A, Worrall D, Giguel F, Piechocka-Trocha A, Atyeo C, Fischinger S, Chan A, Flaherty KT, Hall K, Dougan M, Ryan ET, Gillespie E, Chishti R, Li Y, Jilg N, Hanidziar D, Baron RM, Baden L, Tsibris AM, Armstrong KA, Kuritzkes DR, Alter G, Walker BD, Yu X, Li JZ, Massachusetts Consortium for Pathogen Readiness. 2020. SARS-CoV-2 viral load is associated with increased disease severity and mortality. Nat Commun 11:5493. https://doi.org/10.1038/s41467-020-19057-5.

25. Peters W, Scott HM, Chambers HF, Flynn JL, Charo IF, Ernst JD. 2001. Chemokine receptor 2 serves an early and essential role in resistance to Mycobacterium tuberculosis. Proc Natl Acad Sci U S A 98:7958–7963. https://doi.org/10.1073/pnas.131207398.

26. Roy RM, Wüthrich M, Klein BS. 2012. Chitin elicits CCL2 from airway epithelial cells and induces CCR2-dependent innate allergic inflammation in the lung. J Immunol 189:2545–2552. https://doi.org/10.4049/jimmunol.1200689.

27. Liegeois M, Legrand C, Desmet CJ, Marichal T, Bureau F. 2018. The interstitial macrophage: a long-neglected piece in the puzzle of lung immunity. Cell Immunol 330:91–96. https://doi.org/10.1016/j.cellimm.2018.02.001.

28. Guilliams M, De Kleer I, Henri S, Post S, Vanhoutte L, De Prijck S, Deswarte K, Malissen B, Hammad H, Lambrecht BN. 2013. Alveolar macrophages develop from fetal monocytes that differentiate into long-lived cells in the first week of life via GM-CSF. J Exp Med 210:1977–1992. https://doi.org/10.1084/jem.20131199.

29. Hashimoto D, Chow A, Noizat C, Teo P, Beasley MB, Leboeuf M, Becker CD, See P, Price J, Lucas D, Greter M, Mortha A, Boyer SW, Forsberg EC, Tanaka M, van Rooijen N, García-Sastre A, Stanley ER, Ginhoux F, Frenette PS, Merad M. 2013. Tissue-resident macrophages self-maintain locally throughout adult life with minimal contribution from circulating monocytes. Immunity 38:792–804. https://doi.org/10.1016/j.immuni.2013.04.004.

30. Yona S, Kim K-W, Wolf Y, Mildner A, Varol D, Breker M, Strauss-Ayali D, Viukov S, Guilliams M, Misharin A, Hume DA, Perlman H, Malissen B, Zelzer E, Jung S. 2013. Fate mapping reveals origins and dynamics of monocytes and tissue macrophages under homeostasis. Immunity 38:79–91. https://doi.org/10.1016/j.immuni.2012.12.001.

31. Nakano H, Lyons-Cohen MR, Whitehead GS, Nakano K, Cook DN. 2017. Distinct functions of CXCR4, CCR2, and CX3CR1 direct dendritic cell precursors from the bone marrow to the lung. J Leukoc Biol 101:1143–1153. https://doi.org/10.1189/jlb.1A0616-285R.

32. Herold S, Steinmueller M, von Wulffen W, Cakarova L, Pinto R, Pleschka S, Mack M, Kuziel WA, Corazza N, Brunner T, Seeger W, Lohmeyer J. 2008. Lung epithelial apoptosis in influenza virus pneumonia: the role of macrophage-expressed TNF-related apoptosis-inducing ligand. J Exp Med 205:3065–3077. https://doi.org/10.1084/jem.20080201.

33. Grant RA, Morales-Nebreda L, Markov NS, Swaminathan S, Querrey M, Guzman ER, Abbott DA, Donnelly HK, Donayre A, Goldberg IA, Klug ZM, Borkowski N, Lu Z, Kihshen H, Politanska Y, Sichizya L, Kang M, Shilatifard A, Qi C, Lomasney JW, Argento AC, Kruser JM, Malsin ES, Pickens CO, Smith SB, Walter JM, Pawlowski AE, Schneider D, Nannapaneni P, Abdala-Valencia H, Bharat A, Gottardi CJ, Budinger GRS, Misharin AV, Singer BD, Wunderink RG, NU SCRIPT Study Investigators. 2021. Circuits between infected macrophages and T cells in SARS-CoV-2 pneumonia. Nature 590:635–641. https://doi.org/10.1038/s41586-020-03148-w.

34. Wauters E, Van Mol P, Garg AD, Jansen S, Van Herck Y, Vanderbeke L, Bassez A, Boeckx B, Malengier-Devlies B, Timmerman A, Van Brussel T, Van Buyten T, Schepers R, Heylen E, Dauwe D, Dooms C, Gunst J, Hermans G, Meersseman P, Testelmans D, Yserbyt J, Tejpar S, De Wever W, Matthys P, CONTAGIOUS Collaborators, Neyts J, Wauters J, Qian J, Lambrechts D. 2021. Discriminating mild from critical COVID-19 by innate and adaptive immune single-cell profiling of bronchoalveolar lavages. Cell Res 31:272–290. https://doi.org/10.1038/s41422-020-00455-9.